Optimizing Bionic Blades for Multi-blade Centrifugal Fans: Asymmetric Thickness Inspired by Carangiform Fish

Y. Liu and Q. Yuan[†]

School of Energy and Power Engineering, Xi'an Jiaotong University, Xi'an, Shaanxi, 710049, China

†Corresponding Author Email: qyuan@xjtu.edu.cn

ABSTRACT

Multi-blade centrifugal fans find wide application across various fields, with their internal airflow exhibiting complex turbulent behavior in three dimensions. Historically, blade optimization relied on constant thickness airfoils, limiting the effectiveness of optimization efforts. However, marine organisms have developed airfoil structures with highly efficient drag reduction, offering a novel approach to optimizing multi-blade centrifugal fans. This study proposes an airfoil optimization design method utilizing variable-thickness airfoils to maintain consistent pressure surface leading-edge parameters. By integrating the Non-dominated Sorting Genetic Algorithm II with biomimetic optimization design, performance improvements are achieved. The study constructs an asymmetric bionic blade using a Bezier curve to fit the mean camber line of the blade. Experimental testing validates the optimized fan's performance, demonstrating the effectiveness of the proposed design approach in reducing the unsteady interaction between the impeller and the volute tongue. This reduction significantly diminishes sound pressure fluctuations on the blade surface. Notably, at the maximum volume flow rate, the optimized fan featuring the asymmetric bionic blade exhibits a remarkable enhancement, with a 10.5% increase in volume flow rate and a notable 1.7 dB reduction in noise compared to the original fan configuration.

1. INTRODUCTION

In recent years, the efficient utilization and sustainable development of energy have emerged as prominent themes in social research. Multi-blade centrifugal fans find widespread application across various industries due to their compact size and high flow coefficient. Given their role as core power components, optimizing their structure and enhancing performance are pivotal for reducing energy consumption. However, the impeller, being the sole rotating component, can experience significant interference with the stationary parts during operation. The internal airflow within centrifugal fans is characterized by complex and unsteady turbulent behavior, influenced by the fan's structural characteristics (Kim et al., 2013). The wake generated by upstream blades can notably affect airflow in downstream passages.

Optimizing the impeller involves two primary aspects: blade parameters and impeller parameters. Blade parameters include variables such as inlet and outlet installation angles (Zhou et al., 2021). Conversely, impeller parameters encompass considerations such as the number of blades, inner and outer diameter, and impeller height (Darvish et al., 2015). Typically, parameters with the most significant influence are prioritized during optimization efforts. Studies have shown that increasing the blade count and outlet angle can improve flow separation within the impeller channel. Albanesi et al. (2023) proposed a polynomial parameterization strategy for blade chord and torsion distribution in axial flow fans, resulting in an 18% enhancement in fan efficiency while adhering to all design constraints. Wang et al. (2020) investigated the effects of full and partial blade cutting, suggesting that judicious blade cutting could mitigate inactive areas near the front plate. However, variable-thickness airfoil blades remained vulnerable to leading-edge damage, potentially compromising aerodynamic performance.

Lin & Huang (2002) explored blade airfoil design using a low-speed NACA 4412 airfoil on the blades, effectively countering flow separation and enhancing fan efficiency. Jiang et al. (2019) employed the random modulation method to create a non-uniform spacing for

impeller blades, dispersing sound energy to specific frequencies and reducing noise emissions. Wang et al. (2018) investigated the integration of bionic reconstruction structures inspired by owl wing section airfoils into centrifugal fan blades, which mitigated vortex generation and pressure pulsation. Conversely, Yang et al. (2020) introduced a double-arc blade, resulting in elevated fan pressure and increased efficiency. Qi et al. (2009) conducted experimental inquiries, highlighting that optimal clearance between the volute tongue and hub significantly reduces noise. Gérard et al. (2013) addressed tonal noise control by introducing an airflow obstruction, observing secondary radiating noise equal in magnitude to primary noise but opposite in phase. Tian et al. (2022) pursued a bionic design of axial fan blades inspired by butterfly wings. Wang et al. (2021) focused on optimizing axial flow, rendering it more uniform in fan configurations. Liu et al. (2023) established three-dimensional biomimetic volute tongues based on the wave leading-edge structure of humpback whale fins, effectively suppressing leading-edge separation vortices, wake vortex shedding, and reducing noise. Lei et al. (2023) designed a biomimetic fan blade based on owl wing profiles, effectively reducing mid to low frequency discrete fan noise. These studies collectively underscore the potential of bionic design to enhance aerodynamic performance.

Marine organisms, as the earliest known true bone vertebrates on Earth, have developed efficient swimming mechanisms through millions of years of natural evolution. They maintain high swimming efficiency and low energy consumption during continuous swimming while also exhibiting high burst speed and mobility. These remarkable characteristics provide valuable inspiration for bionic engineering design (Tytell, 2007; Dong & Dou, 2021). For fast-swimming fish or those undertaking long migrations, even minor energy savings can be crucial. The streamlined body of tuna, for instance, enables swift and efficient swimming during Pacific migration. During swimming, the fish can generate thrust not only through low drag, but also by utilizing the recoil motion of the wing cross-section and body to improve thrust generation efficiency. In modern wing shape design, the two-dimensional horizontal section of the fish body is often employed as an airfoil to minimize drag.

Fish swimming is characterized by dynamic features emphasizing fluid propulsion. Positive pressure exerted on the body during swimming contributes significantly to forward motion (Müller et al., 1997; Wise et al., 2018). Additionally, airfoils can generate propulsion directly through their shape and leading-edge suction (Feilich, 2016; Menon & Mittal 2019). Fish swimming modes are broadly classified into eel and carangiform modes (Sane, 2003). In the carangiform mode, fish oscillate the lower half or less of their bodies to enhance swimming efficiency (Anderson et al., 2001). Turkyilmazoglu et al. (1999) and Turkyilmazoglu (2002a, b) analyzed the trailing-edge interaction zone, indicating flow separation occurring beyond critical values of thickness and aspect ratio parameters. Additionally, the forward direction of the fish body generates a large area of negative pressure (Borazjani & Sotiropoulos, 2008; Liu et al., 2017). Studies have shown that bluegill sunfish and brook trout utilize a leading-edge suction mechanism to generate negative pressure in the anterior part of the body during carangiform swimming (Lucas et al., 2020).

This negative pressure significantly contributes to the propulsion of the fish's body, accounting for up to 28% of the total thrust. These findings provided a foundation for researchers to develop bionic designs for fluid machine blades based on fish body contours, yielding promising results. For instance, Xiong et al. (2018) applied the streamlined profile of carangiform fish to the blades, effectively reducing flow separation in the impeller passage. Wang et al. (2023) designed a strongly curved biomimetic blade based on the C-type starting characteristics of fish, which can enhance the starting performance of fans and reduce noise. Additionally, Yan et al. (2020, 2021) developed symmetric and asymmetric bionic airfoils. The study revealed that the asymmetric bionic airfoil design produced significantly higher head and efficiency for the water jet pump compared to the symmetric bionic airfoil design. The findings from these studies have significant implications for reducing the energy consumption associated with fluid or media transportation.

Inspired by the suction mechanism at the leading-edge of carangiform fish, this study introduces a method for optimizing variable-thickness blades for multi-blade centrifugal fans. Initially, a two-dimensional airfoil with a bionic thickness distribution is generated, followed by the application of a third-order Bezier curve to fit the mean camber line of the blade. Subsequently, the NSGA-II (Non-dominated Sorting Genetic Algorithm II) algorithm is employed to optimize the blade design using the asymmetric bionic airfoil. This study lays the groundwork and offers technical insights for enhancing the aerodynamic performance of fans through bionic blade optimization.

2. GEOMETRIC MODEL

2.1 Construction of Asymmetric Bionic Two-Dimensional Airfoil Model

This study proposes a method to construct a bionic blade using the contour of carangiform fish from the head to the tail handle. The contour is obtained by extracting characteristic structures from the fish body according to reference (Gu, 2010), where the horizontal profile is shown in Fig. 1. The contour comprises an elliptical curve, parabolic curve, and straight line from the head to the tail. The bionic airfoil shape is symmetrically distributed. Equation (1) represents the one-sided contour equation of the horizontal section of the fish body:

$$y(x) = \begin{cases} \dfrac{6}{35}\sqrt{0.035^2 - x^2}, & -0.035 \le x \le 0 \\[2mm] \sqrt{\dfrac{0.05625 - x}{1562.5}}, & 0 \le x < 0.05 \\[2mm] \dfrac{2}{15}(0.065 - x), & 0.05 \le x < 0.065 \end{cases} \tag{1}$$

(a)

(b)
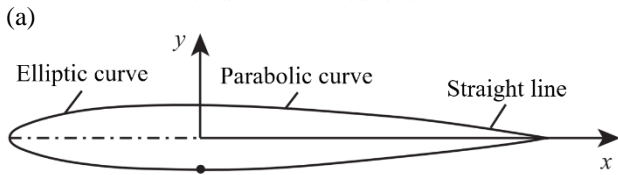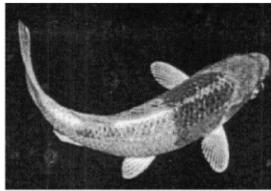
Fig. 1 Horizontal section structure of fish body: (a) Fish body contour, (b) Horizontal profile curve

(a)
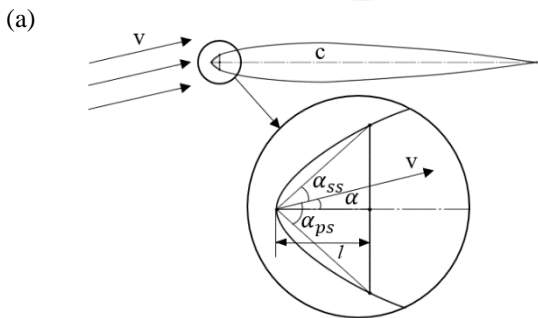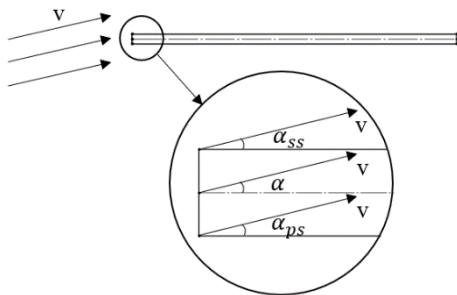
(b)

Fig. 2 Inlet angle of airfoil leading-edge airflow: (a) Constant thickness airfoil, (b) Variable-thickness airfoil

In the context of aerodynamics, the angle formed between the direction of airflow and the chord length of an airfoil is commonly known as the angle of attack, denoted by α, as shown in Fig. 2. In airfoils with constant thickness, $\alpha = \alpha_{ps} = \alpha_{ss}$. However, for variable-thickness airfoils, the included angle between the surface and the incoming airflow is different from the angle of attack. Hence, for a more precise depiction of airflow dynamics at the forefront of variable-thickness airfoils, we define the airflow's inlet angle on the pressure surface, denoted as α_{ps}, as the angle formed between the airfoil's pressure surface leading-edge and the incoming airflow. Similarly, the airflow's inlet angle on the suction surface, denoted as α_{ss}, is defined as the angle between the suction surface leading-edge and the incoming airflow. In this context, 'c' signifies the chord length, and 'l' is a parameter set at $0.025c$, as shown in Table 1. Consequently, $\alpha = (\alpha_{ps}-\alpha_{ss})/2$, as shown in Fig. 2.

Here, we present a methodological refinement whereby the pressure surface attributes are adjusted in accordance with the thickness distribution of a bionic

Table 1 Main characteristic of airfoil

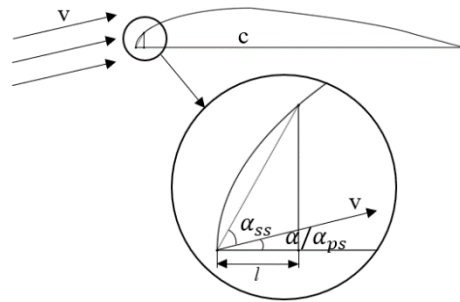| Characteristic parameters	Value
Maximum relative thickness	$0.12c$
Maximum relative thickness position	$0.35c$

Fig. 3 Asymmetric bionic two-dimensional airfoil

airfoil, thereby harmonizing the inlet angle of airflow across the pressure surface with the designated angle of attack. An asymmetric bionic two-dimensional airfoil model is constructed, as shown in Fig. 3, with $\alpha = \alpha_{ps}$. The profile equation of the asymmetric bionic airfoil is given by equation $g(x)$ using Eq. (1):

$$g(x) = 2y(x) \tag{2}$$

2.2 Construction of Asymmetric Bionic Blade Model

The components of the fan are shown in Fig. 4, with the impeller being the focus of analysis. Constructed from molded plastic, the impeller features a fixed center plate, with impellers symmetrically arranged on either side at a 1:1 width ratio. Adhering to a staggered configuration, the impeller blades exhibit a displacement degree equating to half the axial spacing angle, all while oriented forward. The primary structural attributes of the original impeller are detailed in Table 2, offering comprehensive insights into its foundational design characteristics.
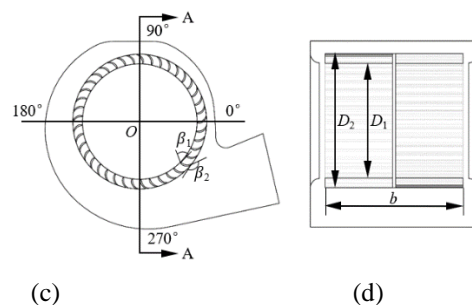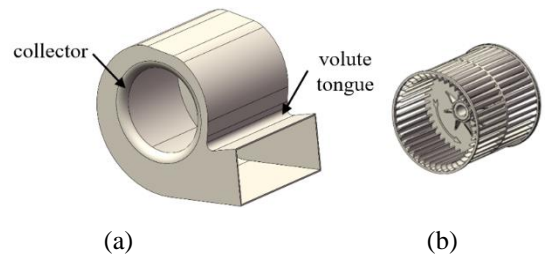

(a)   (b)

(c)   (d)

Fig. 4 Structural of multi-blade centrifugal fan: (a) Volute, (b) Impeller, (c) Sketch map, (d) Section A-A.

Table 2 Basic parameters of impeller

Parameters	Value
Inner diameter D_1/mm	120.00
Outer diameter D_2/mm	138.60
Width of impeller b/mm	143.30
Number of blades Z	41
Inlet installation angle β_1/°	90.00
Outlet installation angle β_2/°	157.70

Fig. 5 Optimal design flow chart of asymmetric bionic blade

Fig. 6 Geometric parameterization of mean camber line in constant thickness blade

Table 3 Parameters design of blade mean camber line

Parameters	Minimum value	Maximum value
Inlet installation angle of blade β_1/°	45.00	80.00
Length of polygon L_1/mm	4.00	7.00
Outlet installation angle of blade β_2/°	160.00	175.00
Length of polygon L_2/mm	3.00	6.00
Center angle of blade γ_1/°	3.50	5.80

Figure 5 illustrates the flowchart delineating the optimal design process for asymmetric bionic blades. This procedural framework comprises two principal phases. Initially, the establishment of a parametric model for the mean camber line of a constant thickness blade is executed, achieved through the utilization of a third-order Bezier curve. Following this, optimization endeavors are directed toward the constant thickness blade, leveraging the asymmetric bionic thickness distribution. The outcome of this optimization endeavor yields an asymmetric bionic blade characterized by variable thickness, thus encapsulating the essence of bionic design principles.

Utilizing the current blade parameters as fundamental variables proves intuitively and efficiently viable from a control standpoint. All control points (V_1–V_4) are designed, as shown in Fig. 6. The V_1 point is fixed and coincides with the inner diameter of the impeller. The inlet installation angle β_1 and the length of the polygon L_1 are the control parameters of the V_2 point, describing the basic parameters of the blade leading-edge. The outlet installation angle β_2 and the length of the polygon L_2 are the control parameters of the V_3 point, describing the basic parameters of the blade trailing-edge. The V_4 point moves circumferentially on the outer diameter of the impeller. The blade center angle γ_1 is the control parameter of the V_4 point, describing the total degree of blade bending. The form of the blade is delineated through the manipulation of these four points, as detailed in Table 3. Employing a

Latin hypercube sampling strategy, the test design is structured. Utilizing Isight's vision design platform, 50 sets of single circular arc schemes with constant thickness blades are generated, as elucidated by Qiu et al. (2021). Figure 7 illustrates the spatial arrangement of the design parameters of the sampled points. Inspection of the figure reveals a satisfactory uniformity in the spatial distribution of each parameter, effectively covering the entire parameter space and ensuring the representativeness of the design samples.

The optimization parameters governing constant-thickness blades show significant alignment with the design parameters of the mean camber line, facilitating the efficient realization of optimization objectives. However, complexities arise when integrating design parameters encompassing blade inlet and outlet installation angles, particularly in aligning them with the parameters of the pressure and suction surfaces of variable-thickness airfoils, especially the pressure surface predominantly serving gas flow. Consequently, transitioning from a constant thickness to a variable-thickness blade may inadvertently alter the inlet airflow angle on the pressure surface while diminishing the outlet airflow angle, potentially impeding fan performance enhancement.

As shown in Fig. 8 (b), the inlet and outlet flow angles of the pressure and suction surfaces of blades with non-uniform thickness exhibit discrepancies with the installation angles at the inlet and outlet. Specifically, the airflow inlet angle β_{1ps} on the blade pressure surface is greater than β_1, whereas the inlet angle of airflow on the suction surface, denoted as β_{1ss}, is less than β_1. Furthermore, the air outlet angle β_{2ps} on the blade pressure surface is smaller than β_2, whereas the outflow corner
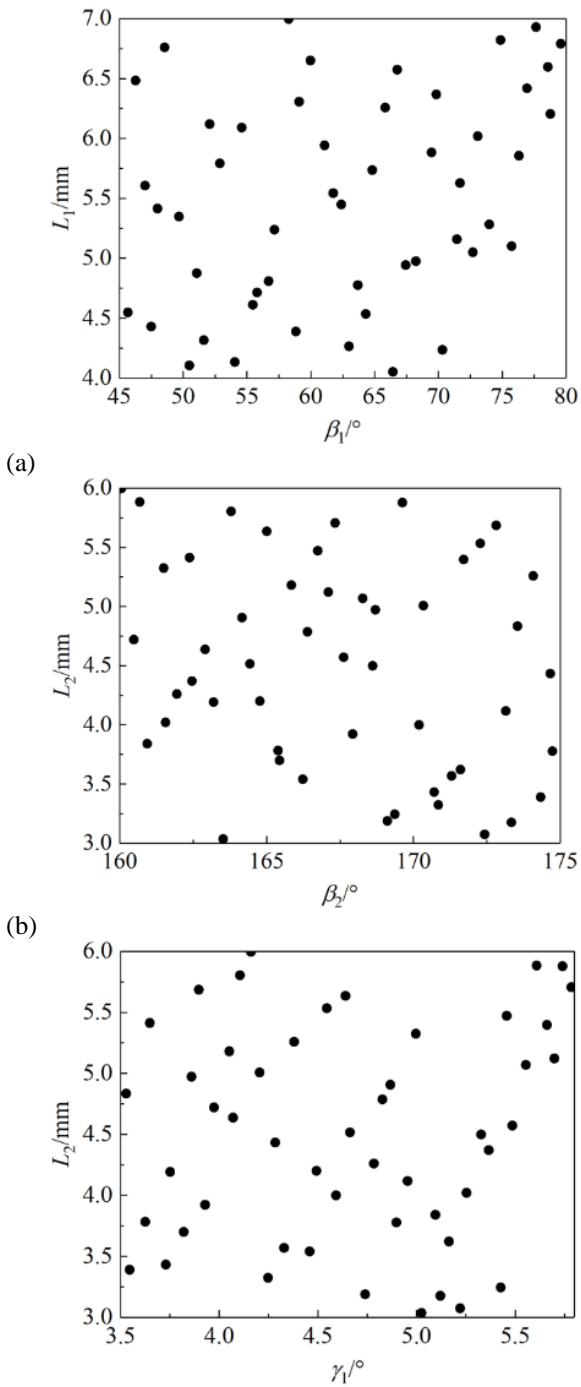
(a)

(b)

(c)

Fig. 7 Spatial distribution of design parameters of mean camber line: (a) β_1-L_1, (b) β_2-L_2, (c) γ_1-L_2
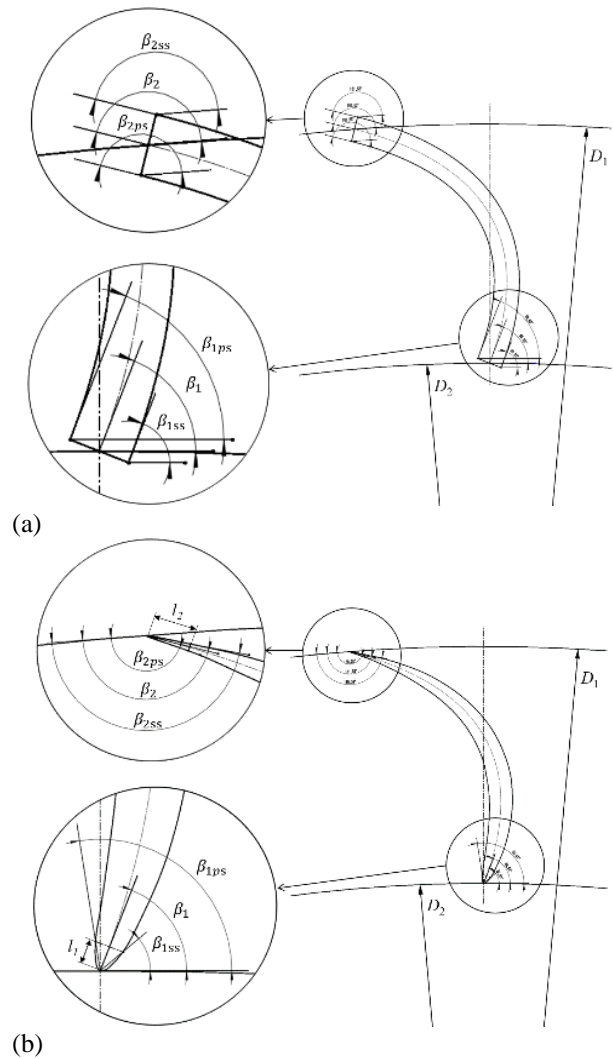

(a)

(b)

Fig. 8 Installation angle of blade inlet and outlet and airflow angle parameters of suction pressure surface: (a) Constant thickness airfoil blade, (b) Variable-thickness airfoil blade

angle β_{2ss} on the suction surface exceeds β_2. The feature length, represented by l_1, amounts to 0.025 times the length of the central arc, whereas the feature length l_2 equates to 0.05 times the length of the central arc.

To address this challenge and uphold the coherence of blade profile optimization parameters, this study advocates keeping the inlet and outlet airflow angles on the blade's pressure surface unchanged while implementing a bionic thickness distribution on the suction surface to craft an asymmetric bionic blade. To this end, the proposed approach employs a variable-thickness blade featuring a bionic thickness distribution, leveraging the suction effect akin to a fish body's leading-edge to mitigate flow separation on the blade's suction surface.

This study introduces an innovative approach to fabricate an asymmetric bionic blade, drawing inspiration from the contour of a fish body. Illustrated in Fig. 1, the horizontal sectional structure of the fish body comprises ellipses, parabolas, and straight lines. In the devised methodology, the contour is proportionally scaled to align the arc length with that of the blade's mean camber line. Through a comprehensive analysis of the fish body's contour equation, the thickness distribution along the chord is derived and discretized to match the radius of the characteristic circle. Subsequently, the bionic blade's contour is formulated as the tangent envelope of the inscribed circle. Diverging from conventional symmetric bionic blades, the proposed asymmetric counterpart situates all inscribed circles tangentially on the suction surface of the mean camber line, employing a spline curve to envelop the tangent plane, as shown in Fig. 9. This methodological innovation facilitates the construction of an optimized blade profile, promising enhanced performance characteristics.
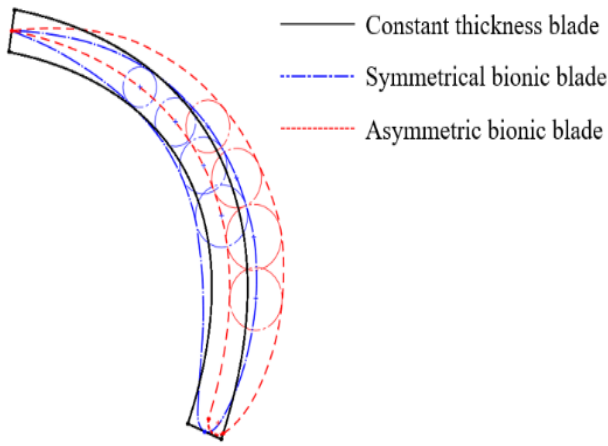
Fig. 9 Schematic diagram of blade structure comparison

Fig. 10 Numerical calculation model

Fig. 11 Grid independence

3. NUMERICAL METHOD AND EXPERIMENTAL TEST

3.1 Numerical Model

The Large Eddy Simulation (LES) method can provide more accurate noise prediction. However, its use is limited by the large computational effort required for models with complex structures. To overcome this limitation, the Realizable *k-ε* model has been introduced, which incorporates relevant expressions of curvature and rotation, making it better suited for situations involving rotation, mixing, and separation (Zhou et al., 2017). The equation is:

$$\frac{\partial(\rho k)}{\partial t} + \frac{\partial(\rho k u_i)}{\partial x_i} = \frac{\partial}{\partial x_j}\left[\left(\mu + \frac{\mu_t}{\sigma_k}\right)\frac{\partial k}{\partial x_j}\right] + G_k - \beta\varepsilon \quad (3)$$

$$\frac{\partial(\rho\varepsilon)}{\partial t} + \frac{\partial(\rho\varepsilon u_i)}{\partial x_i} = \frac{\partial}{\partial x_j}\left[\left(\mu + \frac{\mu_t}{\sigma_\varepsilon}\right)\frac{\partial\varepsilon}{\partial x_j}\right] + \rho C_1 E\varepsilon - \rho C_2 \frac{\varepsilon^2}{k+\sqrt{v\varepsilon}} \quad (4)$$

The impeller of the fan simulated in this paper is a rotating region. The present study specifically targets the flow noise in multi-blade centrifugal fans, encompassing gas–solid interactions and gas vortex structure motion. In this context, aerodynamic noise serves as the predominant focus. Ffowcs Williams and Hawkings (1969) previously addressed solid–fluid interaction, which is highly applicable to the research examined in this paper. The relevant equation for this is the FW-H equation:

$$\frac{1}{c_0^2}\frac{\partial^2 p'}{\partial t^2} - \nabla^2 p' = \frac{\partial^2}{\partial x_i \partial x_j}\left[T_{ij}H(f)\right] - \frac{\partial}{\partial x_i}\left\{\left[P_{ij}n_j + \rho u_i(u_n - v_n)\right]\delta(f)\right\}$$
$$+ \frac{\partial}{\partial t}\left\{\left[\rho_0 v_n + \rho(u_n - v_n)\right]\delta(f)\right\}$$
$$(5)$$

In this investigation, the fluid domain model was formulated using SolidWorks software, adhering to the fan model shown in Fig. 4. To streamline computational efficiency and ensure mesh quality control, the model underwent necessary simplifications. Employing the ANSYS mesh module, each segment underwent meshing procedures. The impeller area model was meshed with a hexahedral s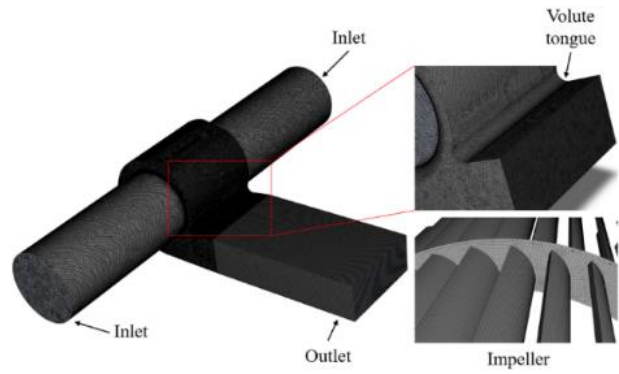tructure, strategically densi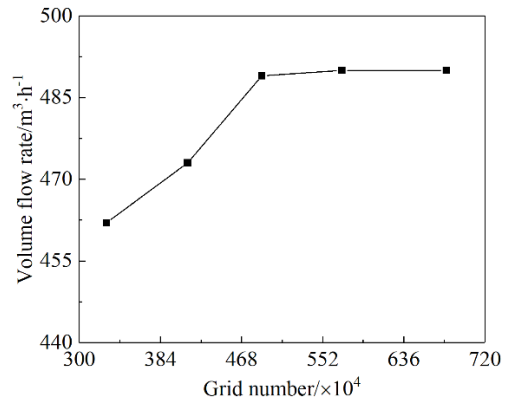fied near-wall boundaries and blade edges for enhanced resolution. Conversely, the volute area adopted a tetrahedral mesh configuration, chosen for its adaptability, with particular emphasis on densification around the volute tongue area to accommodate complex flow patterns. Ensuring adherence to optimal wall treatment, the Y+ value was maintained within the range of 30 to 100 across solid boundaries while interfaces interconnected all constituent parts. The resultant computational model is illustrated in Fig. 10.

To ensure numerical accuracy and expedite computational cycles, grid independence is rigorously evaluated. Flow rate calculations, depicted in Fig. 11, reveal a trend where the fan volume flow rate stabilizes beyond 4.89 million grids, indicating marginal influence of grid number escalation on results. Accordingly, a final grid count of 5.72 million is selected. Additionally, grid orthogonality quality is maintained above 0.25, whereas grid skewness is kept below 0.79, ensuring computational robustness. For the computation of the steady flow field, the Realizable k-ε model is employed as the turbulence model. Boundary conditions are specified accordingly: the inlet is assigned a pressure inlet condition with the total pressure set at 101,325 Pa, whereas the outlet adopts a pressure outlet boundary condition with a static pressure of 101325 Pa. The impeller wall is set as a rotating wall boundary condition.

Following the convergence of steady-state calculation outcomes, transient difference computation is initiated. A time step of 3.26×10^{-5} s is employed, spanning a fan
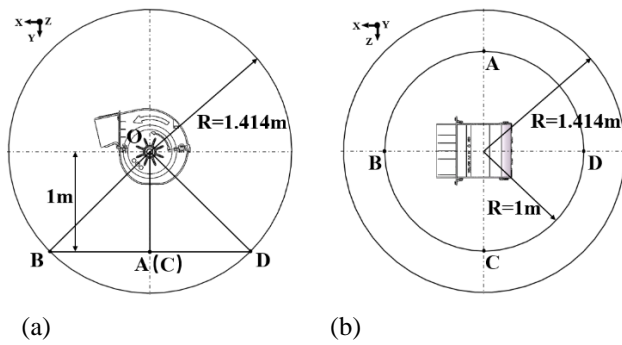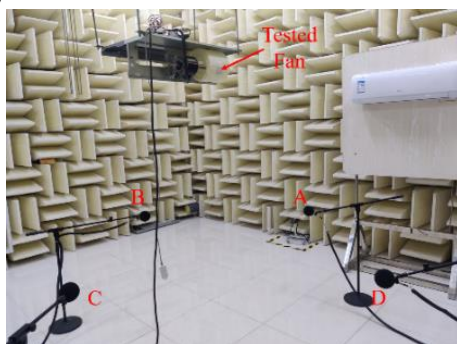
Fig. 12 Schematic diagram of the location of noise measurement points: (a) Front view, (b) Vertical view

Fig. 13 Testing scenario of fan: (a) Aerodynamic performance test, (b) Noise test

operation duration of 0.21 s, corresponding to four complete impeller cycles. Noise sources are identified as wall surfaces, as shown in Fig. 12.

3.2 Experimental Test

Figure 13 (a) presents a schematic diagram of the aerodynamic performance test of the fan. Experimental assessments were conducted at Guangdong Midea Company. During measurement procedures, diverse static pressures are set, and appropriate nozzle diameters are selected based on nozzle flow rates. Conducting a noise assessment for the multi-blade centrifugal fan entails a comprehensive approach. The noise test is administered within a semi-anechoic chamber, shown in Fig. 13(b), ensuring controlled acoustic conditions. Monitoring operations are facilitated using a monitoring sphere with a radius of 1.414 m. Notably, point B is positioned anterior to the fan outlet, ensuring comprehensive noise assessment coverage.
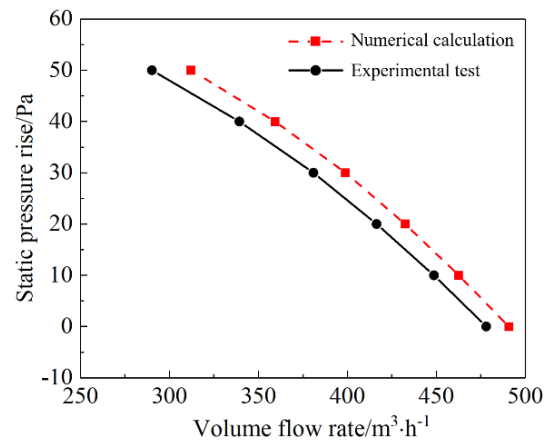

Fig. 14 Performance curves of original fan

Table 4 Error of numerical calculation and experimental test

Parameters	Experimental test	Numerical calculation	Relative Error/%
Volume flow rate/$m^3 \cdot h^{-1}$	478.3	490.7	2.6
Noise/dB	49.3	47.4	3.8

This study conducts numerical simulations across various static pressure operating points, subsequently juxtaposing the findings with experimental data. Performance curves generated through both methodologies, as shown in Fig. 14, reveal strikingly similar trends. Additionally, examination of Table 4 underscores the relative error between volume flow rate and noise levels obtained from experimental tests and numerical computations, standing at 2.6% and 3.8%, respectively. Overall, the numerical predictions exhibit commendable consistency with experimental observations. Hence, the established numerical model emerges as a dependable tool for accurately predicting fan performance.

4. RESULTS AND ANALYSIS

4.1 Aerodynamic Performance Analysis

The current investigation undertakes a CFD analysis focusing on a model operating under the MVP (maximum volume-flow-rate point) condition. Concurrently, a dual-objective Kriging model is constructed, with flow and total pressure efficiency serving as response variables. This Kriging model acts as a pivotal tool, facilitating a functional mapping between design variable inputs and optimization variable outputs. Constructing the Kriging model necessitates a robust dataset comprising numerous sample instances, encapsulating both parameter inputs and resultant outputs (Wang et al., 2011).

In this study, the NSGA-II algorithm, a dual-objective genetic optimization algorithm, is employed to optimize the parameters of the constant thickness blade. A globally optimized agent model is constructed to yield the optimal solution set of dual-objective optimization parameters. By
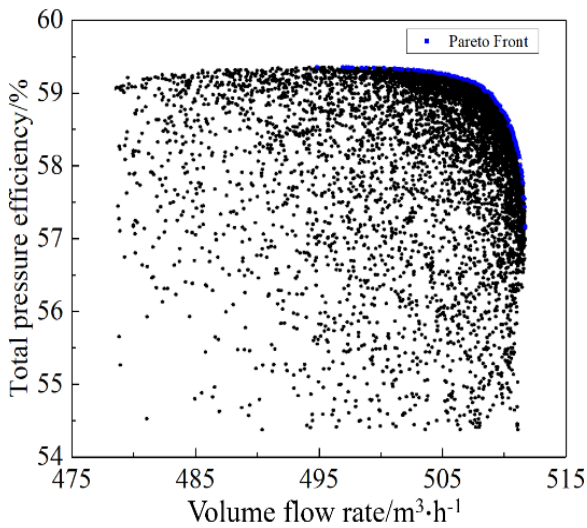
Fig. 15 Pareto front of multi-objective optimization of constant thickness blade

Table 5 Optimal parameters of blade mean camber line

Parameters	Unit	Value
Inlet installation angle of blade β_1	°	69.11
Length of polygon L_1	mm	5.60
Outlet installation angle of bladeβ_2	°	166.50
Length of polygon L_2	mm	4.91
Center angle of blade γ_1	°	4.51

carefully balancing optimization objectives, an optimal non-dominated solution is derived, with key parameters set as follows: a crossover probability of 0.9 for the parent population, a population algebra of 20, and a population size of 400. Moreover, the crossover and mutation distribution indexes are specified as 10.0 and 20.0, respectively. The resulting Pareto front, illustrating the dual-objective optimization of the constant thickness blade, is shown in Fig. 15. The calculated optimal solution stands at 507.6 m³/h and 59.27%, respectively. Furthermore, the optimal design parameters for the bionic reconstruction of the blade are detailed in Table 5.

Table 6 shows the aerodynamic performance calculation results under MVP operating conditions. The total pressure efficiency is calculated by the following formula:

$$\eta = \frac{30P_{t\_vol\_outlet}Q}{\pi nM} \qquad (6)$$

where, η——Total pressure efficiency/%; $P_{t\_vol\_outlet}$—— Total pressure of volute outlet/Pa; Q——Mass flow rate of fan/kg·s⁻¹; n——Rotating speed/r · min⁻¹; M—— Torque/N·m.

Table 6 illustrates the enhancements in volume flow rate resulting from the utilization of three optimized blades for the multi-blade centrifugal fan, each exhibiting varying degrees of improvement. Notably, there is a substantial enhancement in efficiency across all variants. Particularly noteworthy is the fan featuring asymmetric bionic blades, demonstrating the most pronounced performance enhancement. Compared to the original fan configuration, this variant with the maximum volume flow rate elevated by 11.16% and efficiency improved by 5.13%.

For a comprehensive comparison of the performance of the three optimized blades, performance curves are plotted by varying the outlet static pressure. Figure 16 juxtaposes the performance curves of fans equipped with constant thickness, symmetric bionic, and asymmetric bionic blades.

The current investigation conducts a comparative analysis of three blade types: constant thickness, symmetric bionic, and asymmetric bionic blades, with Fig. 16(a) and Fig. 16(b) elucidating the results. Figure 16(a) highlights that the asymmetric bionic blade exhibits superior maximum volume flow rate and maximum static pressure compared to the other blade types. The symmetric bionic blade falls between the constant thickness and asymmetric bionic blades, suggesting potential for further optimization. Examining Fig. 16(b), the fan with asymmetric bionic blades demonstrates the highest overall efficiency, displaying a 1.3%–1.6% enhancement over the symmetric bionic blade at the BEP (Best Efficiency Point). This efficiency advantage is particularly pronounced at the BEP, with marginal alterations observed under low and high flow conditions. Nonetheless, bionic blades present a substantial efficiency advantage over constant thickness blades.

The current investigation delves into the noise characteristics of fans employing diverse optimized blade configurations, maintaining identical volume flow rates, as delineated in Table 7. Given that the volume flow rates of fans equipped with varied optimized blades surpass those of the original blades under the MVP operating condition, noise calculations at uniform volume flow rates were attained through rotational speed reduction. Results reveal distinct levels of noise reduction across the spectrum of optimized blades compared to their original

Table 6 Numerical results of fan with different blades

Scheme	Volume flow rate /m³·h⁻¹	Efficiency/%	Total pressure/Pa	Power /W
Original blade	490.7	57.28	74.76	21.77
Constant thickness airfoil blade	507.6	59.27	79.47	23.10
Symmetric bionic blade	532.8	62.84	88.59	25.47
Asymmetric bionic blade	544.7	62.41	91.71	27.25

Table 7 Noise calculation results of fan with different blades

	Original blade	Constant thickness blade	Symmetric bionic blade	Asymmetric bionic blade
Noise /dB	47.4	46.8	45.3	44.3
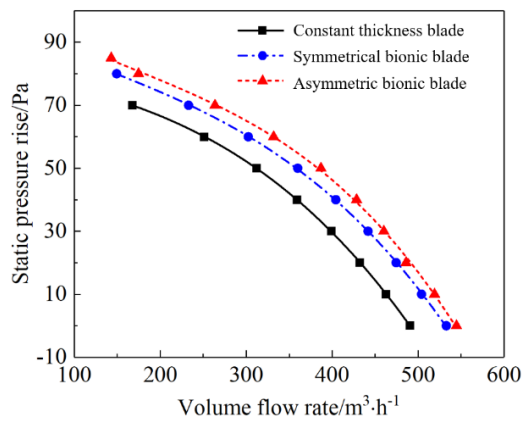
(a)
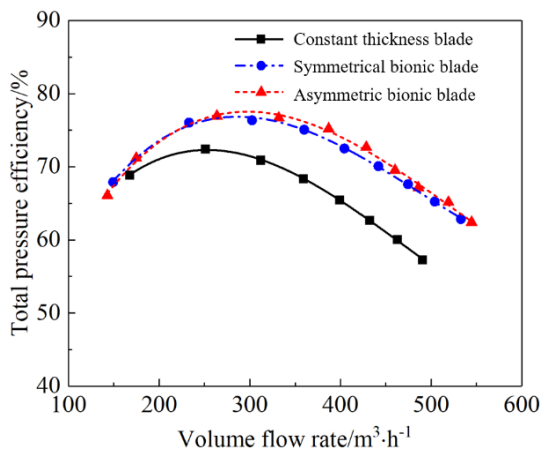
(b)

Fig. 16 Performance curves of fan: (a) Volume flow rate-Pressure curve, (b) Volume flow rate-Efficiency curve

counterparts. Notably, asymmetric bionic blades manifest the most pronounced noise attenuation, registering a reduction of 3.12 dB relative to the original blades. This reduction can be attributed to the streamlined profile inspired by the fish body, effectively mitigating flow separation on the blade surface and consequently dampening noise levels.

Enhancing the performance of an impeller necessitates meticulous attention to both flow uniformity within the impeller passage and the distribution of load capacity. This investigation centers on four designated blade positions situated at 0°, 90°, 180°, and 270° along the circumferential direction, respectively. These specific blade placements are visually depicted in Fig. 17.

Figure 18 presents the load capacity distribution of a fan impeller at the 50% section under MVP operating conditions. Figure 18(a) delineates the blade load capacity distribution of fans equipped with constant thickness, symmetric bionic, and asymmetric bionic blades at the

Fig. 17 Schematic diagram of blade positions

50% section of 0° blade 1. The blade loading capacity is characterized by the pressure difference, denoted as $P_{ps,s}-P_{ss,s}$. Analysis reveals a relatively diminished blade load capacity at the position of blade 1. Specifically, the leading-edge of the blade emerges as a region of high load concentration, contrasted with the trailing-edge categorized as a low load area. Nevertheless, the asymmetric bionic blade demonstrates superior working capacity compared to other variants, with a leading-edge loading mode predominating in blade loading.

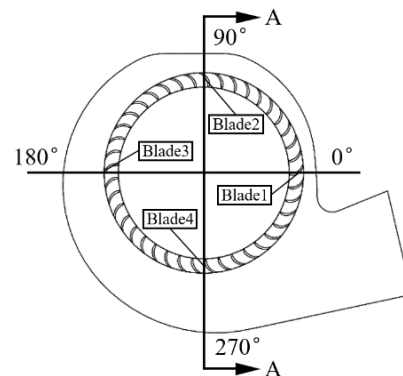Figure 18(b) delineates the blade load capacity distribution of fans equipped with constant thickness, symmetric bionic, and asymmetric bionic blades at the 50% section of 90° blade 2. The loading mode of the blade is typified by loading phenomena at both ends, with unloading occurring at the central position—an attribute intricately linked to the morphological characteristics of the inter-blade flow channel. This loading mode is further influenced by the acceleration and deceleration of airflow within the blade passage. Conversely, discernible loading characteristics are absent in both the constant thickness and symmetric bionic blades. The inlet airflow angle of the symmetrical biomimetic blade increases, thereby inducing a pronounced adverse impact between airflow and the blade's leading-edge, impeding flow within the impeller channel. Moreover, the static pressure on the blade surface notably lags that of the asymmetric bionic blade, with an overall load capacity even inferior to that of the constant thickness blade.

Figure 18(c) and Figure 18(d) show the distribution of blade load capacity at the 50% blade height section for 180° positions 3 and 270° positions 4. Observing these figures reveals distinct loading characteristics among the blade types. While the constant thickness and symmetric bionic blades tend toward leading-edge loading and trailing-edge unloading, the asymmetric bionic blade prominently exhibits trailing-edge loading, with the strongest manifestation occurring at blade 4. Trailing-edge loading serves to diminish the shedding of blade wake vortex, mitigating excitation effects on downstream
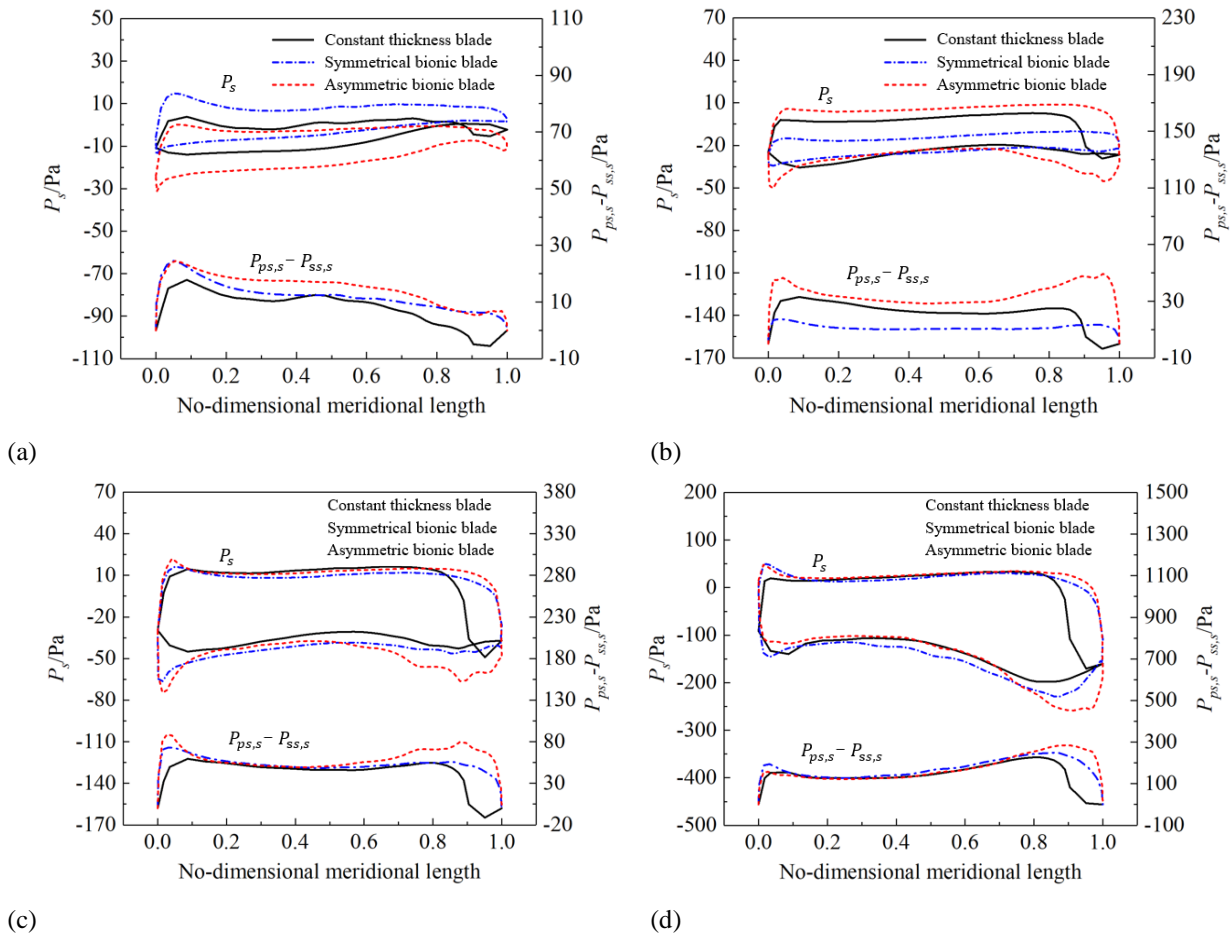
Fig. 18 Blades load capacity distribution: (a) 0°, (b) 90°, (c) 180°, (d) 270°

channels and enhancing impeller efficiency. Notably, at blade 3, the overall working capacity of the three blades exhibits minimal disparity. However, the asymmetric bionic blade highlights a swifter loading initiation, enabling higher blade loading capacity at a reduced circumferential angle—a feature conducive to refining flow dynamics within the volute tongue region.

In Fig. 19, the velocity streamline visualization of the impeller operating under MVP conditions in the optimized multi-blade centrifugal fan is presented. It is evident that the flow dynamics within the blade channel of the asymmetric bionic blade surpass those of the constant thickness and symmetric bionic blades. At the 10% blade height section, a discernible irregular flow distribution and varied degrees of flow separation vortices are observed across different circumferential angles. Conversely, at the 50% and 90% blade height sections, the separation phenomenon within the impeller passage of the asymmetric bionic blade is notably mitigated compared to the constant thickness and symmetric bionic blades, particularly in the proximity of the volute tongue and its downstream region. Through optimization of blade arc parameters and variable-thickness blade distribution, the blade pressure surface's inlet and outlet angles align more closely with airflow, thus diminishing airflow-blade impact. Furthermore, the bionic airfoil modification design on the suction side effectively ameliorates attached vortex shedding on the blade surface while curbing flow

separation at the volute tongue and its downstream passage.

Analysis of vortex behavior within the blade channel of the asymmetric bionic blade indicates that vortex size is minimized at the 50% blade height section, whereas larger vortices manifest at the blade shroud and hub regions. Given that the blade hub side constitutes the principal flow domain of the impeller, it engages in more pronounced interactions with both the volute and volute tongue. Notably, the figure illustrates a distinct truncation of the volute profile, resulting in non-uniform pressure distribution within the volute's flow section and impeding upstream airflow. This phenomenon contributes to notable flow separation observed at the 90% blade height section of the impeller. Analogous patterns are discernible in impellers featuring constant thickness blades and symmetric bionic blades, with no discernible enhancements in flow conditions observed at the 50% blade height section.

The current investigation delved into the radial velocity distribution within the impeller of an optimized multi-blade centrifugal fan operating under MVP conditions, with findings detailed in Fig. 20. Across various blade types, impellers exhibit negative radial velocities, inducing reverse flow at multiple blade height sections. Particularly, the 10% blade height section highlights the most extensive reverse flow region for the asymmetric bionic blade, notably near the volute tongue

(a)   (b)   (c)
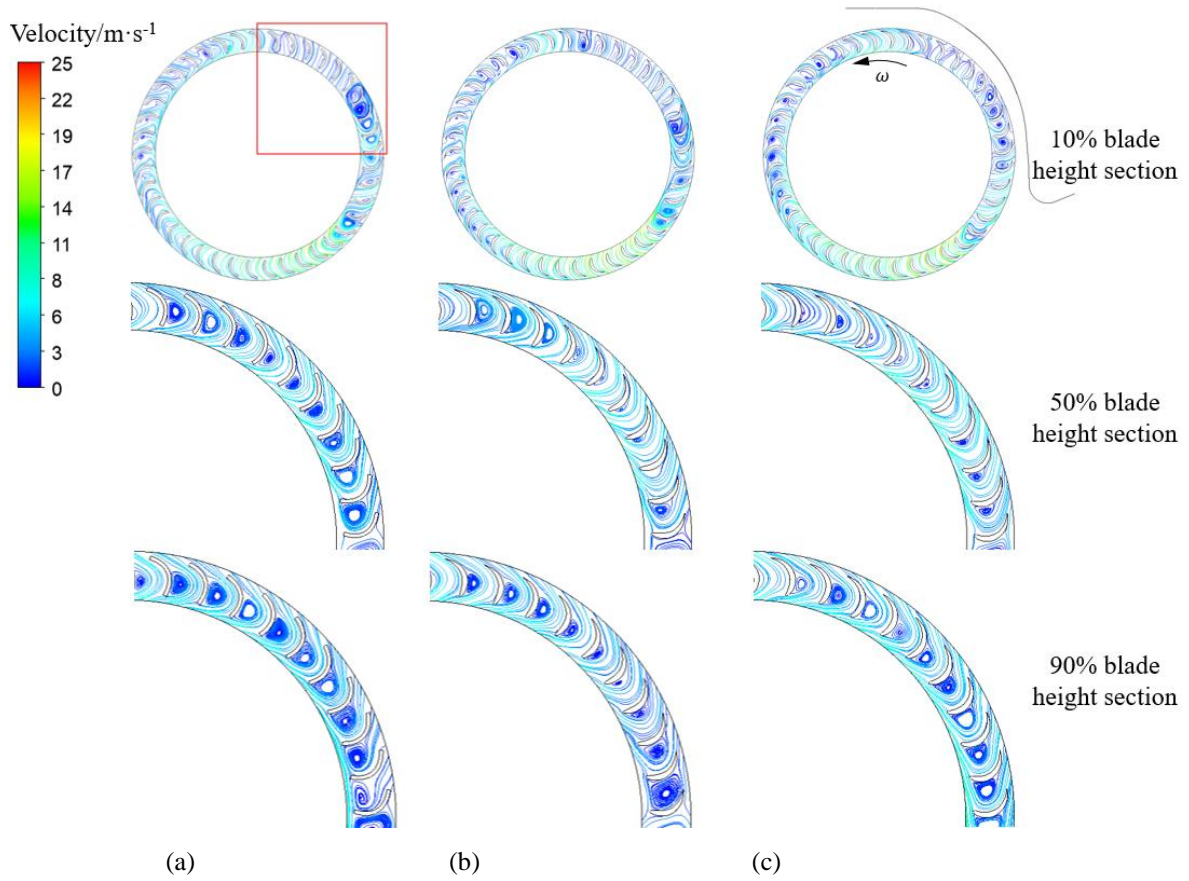
Fig. 19 Velocity streamline of impeller of optimized fan under MVP working condition: (a) Constant thickness blade, (b) Symmetric bionic blade, (c) Asymmetric bionic blade

(a)   (b)   (c)
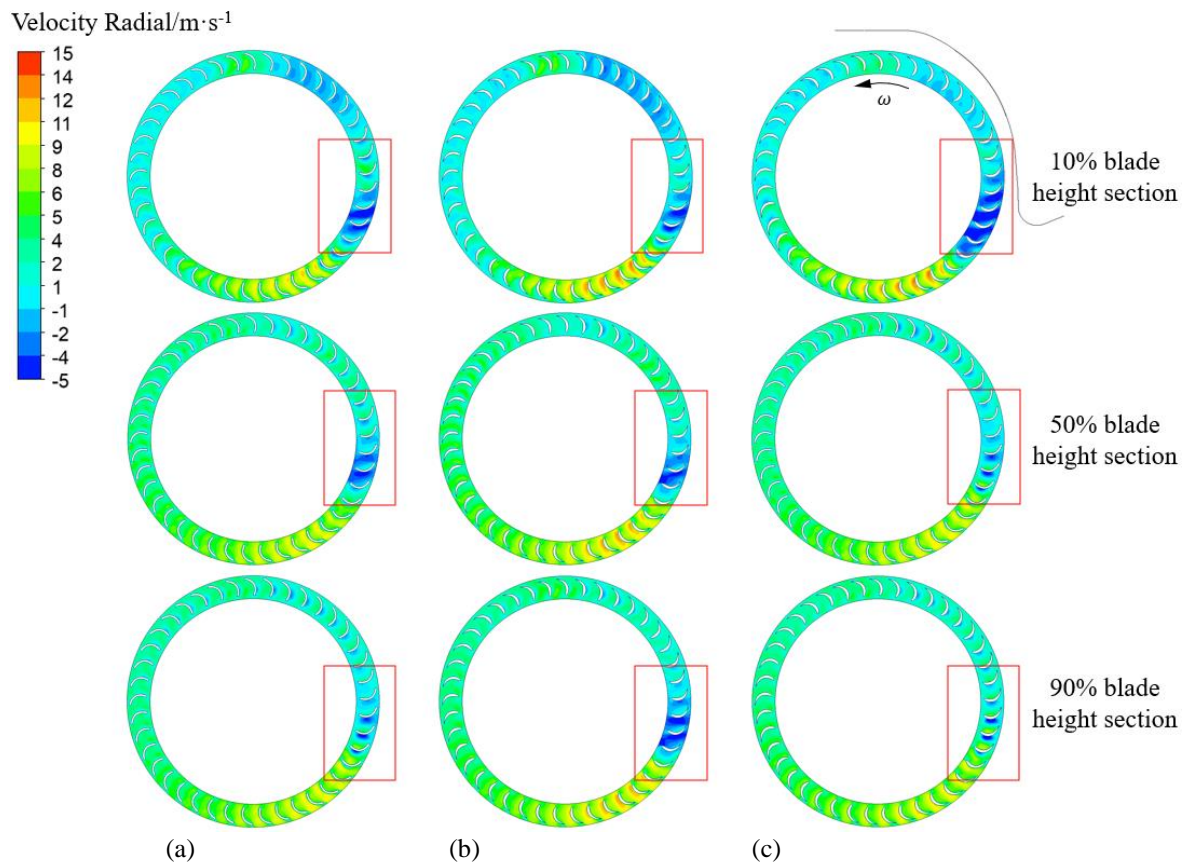
Fig. 20 Radial velocity of optimized multi-blade centrifugal fan under MVP condition: (a) Constant thickness blade, (b) Symmetric bionic blade, (c) Asymmetric bionic blade
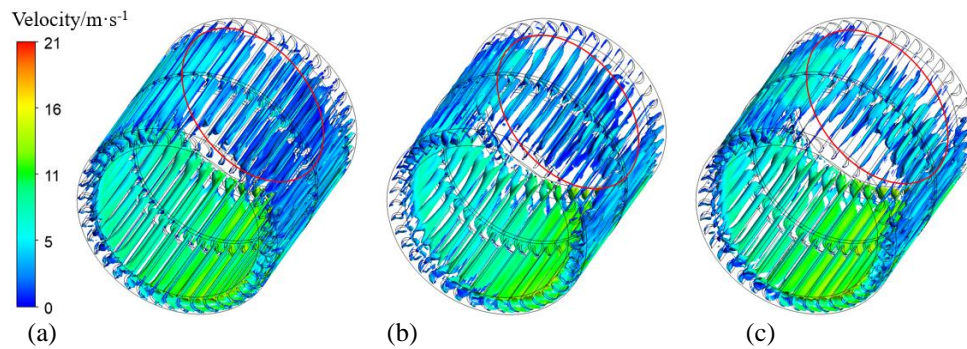
Fig. 21 Vortex core area distribution of the impeller under MVP condition: (a) Constant thickness blade, (b) Symmetric bionic blade, (c) Asymmetric bionic blade

where flow separation is prominent. Conversely, at the 50% and 90% blade height sections, the asymmetric bionic blade demonstrates significant flow condition enhancement compared to constant thickness and symmetric bionic blades, characterized by reduced backflow at the outlet—indicative of heightened operational efficacy.

Viewed through the lens of distinct blade types, the constant thickness blade impeller highlights the most pronounced outlet backflow on the shroud side, gradually diminishing toward the hub side. Similarly, the asymmetric bionic blade impeller exhibits this behavior, albeit with heightened operational efficacy concentrated at the blade hub side. In contrast, the symmetric bionic blade impeller displays a progressive increase in reverse flow from the shroud side to the hub side, likely stemming from the degradation of pressure surface parameters and weakened blade efficacy. Leveraging the trailing-edge load characteristic effectively, the asymmetric bionic blade impeller attains optimal performance, particularly on the advantageous blade hub side. Conversely, the symmetric bionic blade maintains a modest performance level throughout, failing to fully exploit the trailing-edge load characteristic of the impeller. Moreover, it compromises mainstream flow in the blade hub side, exacerbating downstream vortex formation within the volute.

4.2 Noise Characteristics

To uncover the noise mitigation mechanism inherent to the asymmetric bionic blade and delve into the impeller's flow dynamics, an investigation into the noise traits of the fan was conducted. As shown in Fig. 21(a), the vortex core area permeates the impeller passage,

predominantly concentrating at the blade hub side. Notably, heightened vortex intensity is discernible at the volute outlet and tongue, fostering an extensive region of unstable vortex flow. Mitigating this instability holds promise for effectively attenuating the eddy current noise engendered by the fan. Notably, the vortex core area associated with the asymmetric bionic blade exhibits a marked reduction compared to its symmetric counterpart. Following the tenets of vortex sound theory, aerodynamic noise correlates directly with fluid vorticity, suggesting that curtailing the unstable vortex region could notably mitigate the vortex noise arising from the fan.

The study at hand unveils the time-averaged sound pressure level pulsation distribution across the blade surface of the optimized fan under MVP operating conditions, displayed in Fig. 22. Employing time-averaged sound pressure pulsation facilitates a direct portrayal of sound sources (Li et al., 2017). The impeller's principal flow area is delineated as area I, whereas the blade's shroud side corresponds to area II. It is evident that the time-averaged sound pressure level pulsation distribution of the asymmetric bionic blade impeller in both areas I and II markedly diminishes compared to that of the constant thickness blade, indicative of a noteworthy noise reduction efficacy. The suction mechanism inherent to the bionic blade's leading-edge effectively curtails flow separation along the blade surface. Furthermore, between the asymmetric bionic blade's airflow undergoes a sequence of acceleration, deceleration, and re-acceleration, facilitating an enhanced shedding process of separation vortex in the blade wake. This serves to diminish the excitation impact of the separation vortex on the downstream channel, thereby playing a pivotal role in mitigating noise levels within the fan.
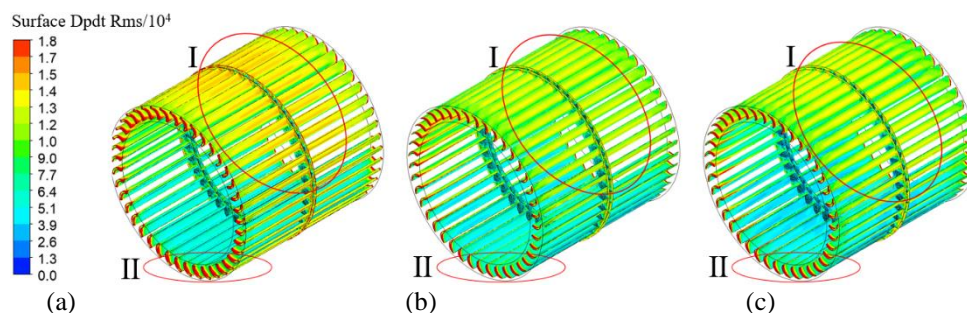

Fig. 22 Sound pressure pulsation on the blade surface under MVP working condition: (a) Constant thickness blade, (b) Symmetric bionic blade, (c) Asymmetric bionic blade
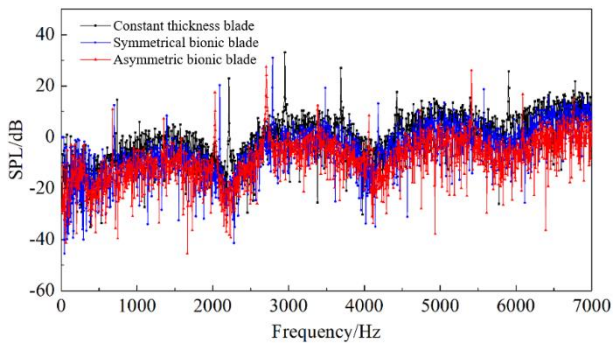
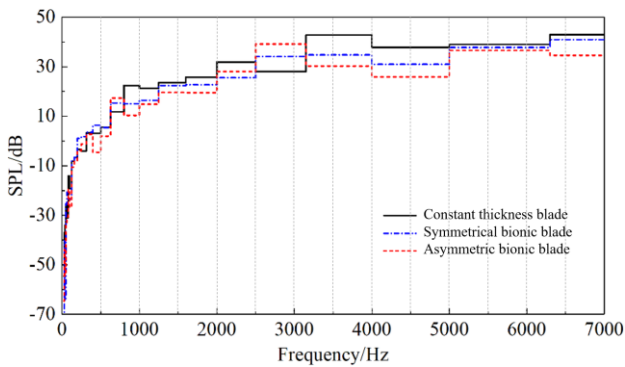**Fig. 23 Noise spectrum distribution at measuring point B under MVP condition**

Fig. 24 1/3 octave frequency spectrum distribution at measuring point B under MVP condition

Table 8 Performance test of fan

Static pressure /Pa	Rotating speed/r·min⁻¹	Volume flow rate of original impeller/m³·h⁻¹	Volume flow rate of bionic impeller/m³·h⁻¹
0	1120	478.3	528.6
10	1120	448.6	493.4
20	1120	416.4	459.6
30	1120	380.9	416.8
40	1120	339.3	374.8
50	1120	290.1	318.2

Table 9 Noise experimental test of fan under the same volume flow rate

Static pressure /Pa	Volume flow rate /m³·h⁻¹	Original impeller		Bionic impeller	
		Rotating speed /r·min⁻¹	Noise /dB	Rotating speed /r·min⁻¹	Noise/ dB
0	478.3	1120	49.3	1025	47.6
0	428.3	1000	45.7	936	44.1
0	402.5	940	43.8	866	42.2
0	357.3	783	38.8	719	37.1
0	326.8	685	34.9	634	33.3
0	302.6	630	31.8	578	30.3

Figure 23 presents the noise spectrum distribution at measurement point B, obtained through Fourier transform. The investigation employs three optimized blades while maintaining a consistent volume flow rate by adjusting the impeller speed. The findings indicate a low sound pressure level within the frequency range of 0 ~ 500 Hz, contrasting with a pronounced increase in sound pressure level within the range of 500 ~ 3000 Hz. Notably, the peak sound pressure level exhibits periodic fluctuations, peaking approximately every 700 Hz across the 0 ~ 3000 Hz frequency range. Moreover, within the 3000 ~ 7000 Hz frequency range, the peak sound pressure level generally demonstrates a decreasing trend. Comparatively, the noise emitted by the fan with asymmetric bionic blades registers lower levels than its constant thickness blade counterpart at each frequency doubling peak, signifying a discernible noise reduction effect.

Figure 24 illustrates the 1/3 octave frequency spectrum distribution of the sound level emanating from a fan respectively equipped with three optimized blades under MVP operating conditions. Notably, the reduction in sound pressure level attributed to the fan employing asymmetric bionic blades exhibits a more pronounced effect above 500 Hz compared to its counterparts. While the symmetric bionic blade impeller demonstrates a lower sound pressure level relative to the constant thickness blade, the extent of reduction is not as remarkable as observed with the asymmetric bionic blade. This observation underscores the enhanced internal flow dynamics achieved with the asymmetric bionic blade fan, facilitated by its distinct bionic airfoil pressure surface,

which upholds the optimized design parameters characteristic of the constant thickness blade. This unique attribute effectively addresses the limitations inherent in the symmetric bionic blade, including its diminished work capacity and constrained noise reduction capabilities.

5. EXPERIMENTAL TEST RESULTS

To validate the efficacy of the asymmetric bionic blade, experimental testing is employed. The test results are shown in Tables 8 and 9. The bionic impeller is crafted from the identical material utilized in the original impeller. Operated by an AC motor, the original impeller rotates at 1120 r·min⁻¹. Adjustment of the AC motor's power supply voltage enables precise control of the rotation speed to attain equivalent volume flow rate conditions. Figure 25
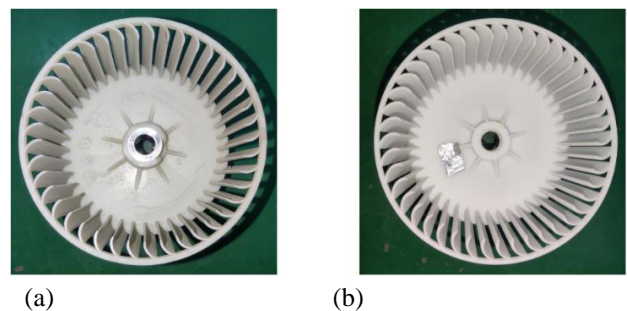

(a)   (b)

Fig. 25 Experimental test impeller: (a) Original impeller, (b) Bionic impeller

illustrates both the original and bionic impellers side by side, with the latter featuring asymmetric bionic blades. A noticeable enhancement in the total volume flow rate of the optimized fan, by approximately 10%, is evident at identical rotational speeds. Concurrently, at equivalent volume flow rates, noise reduction of 1.5–1.7 dB across all settings is observed for the optimized fan. This underscores the favorable noise reduction capabilities of the asymmetric bionic blade.

6. CONCLUSIONS

This study introduces a design methodology for variable-thickness airfoils inspired by the suction mechanism observed in the leading-edge of carangiform fish. This approach guarantees the leading-edge parameters of the pressure surface through the utilization of a two-dimensional airfoil featuring symmetric and asymmetric bionic thickness distribution. Key conclusions derived from this investigation include:

(1) Among the various optimized blades, the asymmetric bionic blade demonstrates distinct trailing-edge loading attributes. Retaining the advantageous pressure surface distribution observed in constant thickness blades, it notably enhances the blade's operational efficacy.

(2) The asymmetric bionic blade effectively mitigates unsteady interaction, leading to a notable suppression of flow separation both at the volute tongue and throughout the downstream channel. Moreover, there is a significant reduction in the time-averaged sound pressure fluctuation at the blade surface.

(3) The integration of the NSGA-II optimization algorithm with a bionic structure in blade design proves instrumental in enhancing the aerodynamic performance of the fan.

(4) Specifically, at the operational point corresponding to the maximum volume flow rate, the fan equipped with asymmetric bionic blades demonstrates a remarkable increase in volume flow rate by 10.5%, accompanied by a reduction in noise by 1.7 dB compared to the original fan configuration.

FUTURE PLANS AND FUTURE WORK

For impeller optimization, the focus was solely on studying the design parameters of the blades, limited to the two-dimensional airfoil structure. Future plans involve optimizing the inner and outer diameters, as well as the blade height parameters of the impeller.

Given the significant uneven flow distribution along the blade height within the impeller of a multi-blade centrifugal fan, there is potential to optimize the three-dimensional design of the blades. This optimization can aim to achieve a more uniform flow inside the impeller and better adaptation to the flow state within the multi-blade centrifugal fan.

CONFLICT OF INTEREST

The authors declare that they have no known competing financial interests or personal relationships that could have appeared to influence the work reported in this paper.

AUTHORS CONTRIBUTION

Yang Liu: Methodology; Numeral Calculations; Conceptualization; Writing – original draft; Formal analysis; Experiment. **Qi Yuan:** Funding acquisition; Conceptualization; Discussion; Writing – review & editing; Validation.

REFERENCES

Albanesi, A. E., Dorella, J. J., Storti, B. A., & Volpe, N. J. A. (2023). A Simulation-based optimization approach for poultry axial exhaust fans to fulfill aerodynamic and mechanical service constraints. *Structural and Multidisciplinary Optimization*, *66*(2), 39. https://doi.org/10.1007/s00158-023-03506-y

Anderson, E. J., McGillis, W. R., & Grosenbaugh, M. A. (2001). The boundary layer of swimming fish. *The Journal of Experimental Biology*, *204*(1), 81–102. https://doi.org/10.1242/jeb.204.1.81

Borazjani, I., & Sotiropoulos, F. (2008). Numerical investigation of the hydrodynamics of carangiform swimming in the transitional and inertial flow regimes. *The Journal of Experimental Biology*, *211*(10), 1541–1558. https://doi.org/10.1242/jeb.015644

Darvish, M., Frank, S., & Paschereit, C. O. (2015). Numerical and experimental study on the tonal noise generation of a radial fan. *Journal of Turbomachinery*, *137*(10), 101005. https://doi.org/10.1115/1.4030498

Dong, X., & Dou, H. S. (2021). Effects of bionic volute tongue bioinspired by leading edge of owl wing and its installation angle on performance of multi-blade centrifugal fan. *Journal of Applied Fluid Mechanics*, *14*(4), 1031–1043. https://doi.org/10.47176/jafm.14.04.31987

Feilich, K. L. (2016). Correlated evolution of body and fin morphology in the cichlid fishes. *Evolution; International Journal of Organic Evolution*, *70*(10), 2247–2267. https://doi.org/10.1111/evo.13021

Ffowcs-Williams, J. E., & Hawkings, D. L. (1969). Sound generation by turbulence and surfaces in arbitrary motion. *Philosophical Transactions of the Royal Society of London. Series A, Mathematical and*

Physical Sciences, *264*(1151), 321–342. https://doi.org/10.1098/rsta.1969.0031

Gérard, A., Besombes, M., Berry, A., Masson, P., & Moreau, S. (2013). Tonal noise control from centrifugal fans using flow control obstructions. *Noise Control Engineering Journal*, *61*(4), 381–388. https://doi.org/10.3397/1/3761032

Gu, B. (2010). *Study on propulsion behavior and swimming trajectory planning of fish using flow field energy* [Unpublished dissertation]. Harbin Institute of Technology.

Jiang, B. Y., Wang, J., Yang, X. P., Wang, W., & Ding, Y. Y. (2019). Tonal noise reduction by unevenly spaced blades in a forward-curved-blades centrifugal fan. *Applied Acoustics*, *146*, 172–183. https://doi.org/10.1016/j.apacoust.2018.11.007

Kim, J. H., Cha, K. H., & Kim, K. Y. (2013). Parametric study on a forward-curved blades centrifugal fan with an impeller separated by an annular plate. *Journal of Mechanical Science and Technology*, *27*(6), 1589–1595. https://doi.org/10.1007/s12206-013-0404-4

Lei, J., Cui, Q., & Qin, G. L. (2023). Performance improvement and noise reduction analysis of multi-blade centrifugal fan imitating long-eared owl wing surface. *Physics of Fluids*, *35*(12), 125147. https://doi.org/10.1063/5.0184598

Li, D., & Liu, X. M. (2017). A comparative study on aerodynamic performance and noise characteristics of two kinds of long-eared owl wing models. *Journal of Mechanical Science and Technology*, *31*(8), 3821–3830. https://doi.org/10.1007/s12206-017-0726-8

Lin, S. C., & Huang, C. L. (2002). An integrated experimental and numerical study of forward–curved centrifugal fan. *Experimental Thermal and Fluid Science*, *26*(5), 421–434. https://doi.org/10.1016/S0894-1777(02)00112-7

Liu, G., Ren, Y., Dong, H., Akanyeti, O., Liao, J. C., & Lauder, G. V. (2017). Computational analysis of vortex dynamics and performance enhancement due to body–fin and fin–fin interactions in fish-like locomotion. *Journal of Fluid Mechanics*, *829*, 65–88. https://doi.org/10.1017/jfm.2017.533

Liu, Y., Yuan, Q., Xu, Z. Q., Wu, L. M., & Liu, X. M. (2023). Bionic volute tongue optimization design of multi-blade centrifugal fan inspired by the wave leading-edge of humpback whale flippers. *Journal of Bionic Engineering*, *20*(5), 2209–2227. https://doi.org/10.1007/s42235-023-00354-w

Lucas, K. N., Lauder, G. V., & Tytell, E. D. (2020). Airfoil-like mechanics generate thrust on the anterior body of swimming fishes. *Proceedings of the National Academy of Sciences of the United States of America*, *117*(19), 10585–10592. https://doi.org/10.1073/pnas.1919055117

Menon, K., & Mittal, R. (2019). Flow physics and dynamics of flow-induced pitch oscillations of an airfoil. *Journal of Fluid Mechanics*, *877*, 582–613. https://doi.org/10.1017/jfm.2019.627

Müller, U. K., Heuvel, B., Stamhuis, E. J., & Videler, J. J. (1997). Fish foot prints: Morphology and energetics of the wake behind a continuously swimming mullet (Chelon labrosus risso). *The Journal of Experimental Biology*, *200*(22), 2893–2906. https://doi.org/10.1242/jeb.200.22.2893

Qi, D. T., Mao, Y. J., Liu, X. L., & Yuan, M. J. (2009). Experimental study on the noise reduction of an industrial forward-curved blades centrifugal fan. *Applied Acoustics*, *70*(8), 1041–1050. https://doi.org/10.1016/j.apacoust.2009.03.002

Qiu, S. W., Xue, Z. G., He, H., Yang, Z., Xia, E. L., Xu, C. C., & Li, L. X. (2021). Multi-objective optimization study on the power cooling performance and the cooling drag of a full-scale vehicle. *Structural and Multidisciplinary Optimization*, *64*(6), 4129–4145. https://doi.org/10.1007/s00158-021-03035-6

Sane, S. P. (2003). The aerodynamics of insect flight. *The Journal of Experimental Biology*, *206*(23), 4191–4208. https://doi.org/10.1242/jeb.00663

Tian, C. Y., Liu, X. M., Wang, J. H., & Xi, G. (2022). Effects of bionic blades inspired by the butterfly wing on the aerodynamic performance and noise of the axial flow fan used in air conditioner. *International Journal of Refrigeration*, *140*, 17–28. https://doi.org/10.1016/j.ijrefrig.2022.04.018

Turkyilmazoglu, M. (2002a). Flow in the vicinity of the trailing edge of Joukowski-type profiles. *Proceedings of the Royal Society of London. Series A: Mathematical, Physical and Engineering Sciences*, *458*(2023), 1653–1672. https://doi.org/10.1098/rspa.2001.0942

Turkyilmazoglu, M. (2002b). The absolute instability of Joukowski-type airfoils. *Theoretical and Computational Fluid Dynamics*, *15*(4), 255–264. https://doi.org/10.1007/s001620100053

Turkyılmazoglu, M., Gajjar, J. S. B., & Ruban, A. I. (1999). The absolute instability of thin wakes in an incompressible/compressible fluid. *Theoretical and Computational Fluid Dynamics*, *13*(2), 91–114. https://doi.org/10.1007/s001620050006

Tytell, E. D. (2007). Do trout swim better than eels? challenges for estimating performance based on the wake of self-propelled bodies. *Experiments in Fluids*, *43*(5), 701–712. https://doi.org/10.1007/s00348-007-0343-x

Wang, G. C., Cheng, A. G., Hu, C. H., & Zhong, Z. H. (2011). Crashworthiness optimization of automobile front structure based on Kriging model. *Automotive Engineering*, *33*, 208–212. https://doi.org/10.19562/j.chinasae.qcgc.2011.03.006

Wang, J. H., Liu, X. M., Tian, C. Y., & Xi, G. (2023). Aerodynamic performance improvement and noise

control for the multi-blade centrifugal fan by using bio-inspired blades. *Energy*, *263*, 125829. https://doi.org/10.1016/j.energy.2022.125829

Wang, K., Ju, Y. P., & Zhang, C. H. (2020). Experimental and numerical investigations on effect of blade trimming on aerodynamic performance of squirrel cage fan. *International Journal of Mechanical Sciences*, *177*, 105579. https://doi.org/10.1016/j.ijmecsci.2020.105579

Wang, K., Ju, Y. P., & Zhang, C. H. (2021). Aerodynamic optimization of forward-curved blade centrifugal fan characterized by inclining bionic volute tongue. *Structural and Multidisciplinary Optimization*, *63*(5), 2493–2507. https://doi.org/10.1007/s00158-020-02801-2

Wang, M. H., Wu, L. M., Liu, X. M., Ma, L., & Li, J. B. (2018). A study on noise reduction of centrifugal fan in air conditioner by using the bionic blade inspired by the owl wing. *Journal of Xi'an Jiaotong University*, *52*, 55–61. https://doi.org/10.7652/xjtuxb201806009

Wise, T. N., Schwalbe, M. A. B., & Tytell, E. D. (2018). Hydrodynamics of linear acceleration in bluegill sunfish, Lepomis macrochirus. *The Journal of Experimental Biology*, *221*(23), jeb190892. https://doi.org/10.1242/jeb.190892

Xiong, Z. Y., Wang, M. H., Liu, X. M., Li, D., & Wang, L. (2018). Study on performance of multi-blade centrifugal fan with bionic blade. *Journal of Xi'an Jiaotong University*, *52*(11), 22–29. https://doi.org/10.7652/xjtuxb201811004

Yan, H., Su, X. Z., Zhang, H. Z., Hang, J. W., Zhou, L., Liu, Z. F., & Wang, Z. J. (2020). Design approach and hydrodynamic characteristics of a novel bionic airfoil. *Ocean Engineering*, *216*, 108076. https://doi.org/10.1016/j.oceaneng.2020.108076

Yan, H., Zhang, H. Z., Zeng, Y. S., Wang, F., & He, X. Y. (2021). Lift-drag characteristics and unsteady cavitating flow of bionic hydrofoil. *Ocean Engineering*, *225*, 108821. https://doi.org/10.1016/j.oceaneng.2021.108821

Yang, X. P., Jiang, B. Y., Wang, J., Huang, Y. G., Yang, W. G., Yuan, K. M., & Shi, X. (2020). Multi-objective optimization of dual-arc blades in a squirrel-cage fan using modified non-dominated sorting genetic algorithm. *Proceedings of the Institution of Mechanical Engineers, Part A: Journal of Power and Energy*, *234*(8), 1053–1068. https://doi.org/10.1177/0957650919898983

Zhou, H., Zhang, M. X., & He, B. J. (2017). Research of wall roughness effects based on Q criterion. *Microfluidics and Nanofluidics*, *21*(7), 114. https://doi.org/10.1007/s10404-017-1951-2

Zhou, S. Q., Zhou, H. X., Yang, K., Dong, H. B., & Gao, Z. L. (2021). Research on blade design method of multi-blade centrifugal fan for building efficient ventilation based on hicks-henne function. *Sustainable Energy Technologies and Assessments*, *43*, 100971. https://doi.org/10.1016/j.seta.2020.100971